



Cite as  
Nano-Micro Lett.  
(2022) 14:224

## Significantly Enhanced Electromagnetic Interference Shielding Performances of Epoxy Nanocomposites with Long-Range Aligned Lamellar Structures

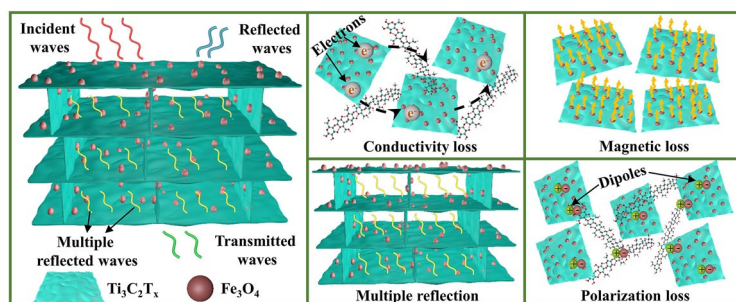
Lei Wang<sup>1,2</sup>, Zhonglei Ma<sup>2</sup>, Hua Qiu<sup>2</sup> ✉, Yali Zhang<sup>2</sup>, Ze Yu<sup>2</sup>, Junwei Gu<sup>2</sup> ✉

Received: 20 August 2022  
Accepted: 7 September 2022  
Published online: 15 November 2022  
© The Author(s) 2022

### HIGHLIGHTS

- $\text{Ti}_3\text{C}_2\text{T}_x@Fe_3O_4/CNF$  aerogels (BTFCAs)/epoxy electromagnetic interference (EMI) shielding nanocomposites with long-range aligned lamellar structures were prepared by bidirectional freezing, freeze-drying and vacuum-assisted impregnation of epoxy resins.
- Successful construction of 3D long-range aligned lamellar structures and electromagnetic synergistic effect could significantly increase the EMI shielding effectiveness and reduce the secondary contamination.
- BTFCA/epoxy EMI shielding nanocomposites possessed outstanding EMI shielding effectiveness of 79 dB, and also presented excellent thermal stabilities and mechanical properties.

**ABSTRACT** High-efficiency electromagnetic interference (EMI) shielding materials are of great importance for electronic equipment reliability, information security and human health. In this work, bidirectionally aligned  $\text{Ti}_3\text{C}_2\text{T}_x@Fe_3O_4/CNF$  aerogels (BTFCAs) were firstly assembled by bidirectional freezing and freeze-drying technique, and the BTFCA/epoxy nanocomposites with long-range aligned lamellar structures were then prepared by vacuum-assisted impregnation of epoxy resins. Benefitting from the successful construction of bidirectionally aligned three-dimensional conductive networks and electromagnetic synergistic effect, when the mass fraction of  $\text{Ti}_3\text{C}_2\text{T}_x$  and  $Fe_3O_4$  are 2.96 and 1.48 wt%, BTFCA/epoxy nanocomposites show outstanding EMI shielding effectiveness of 79 dB, about 10 times of that of blended  $\text{Ti}_3\text{C}_2\text{T}_x@Fe_3O_4/epoxy$  (8 dB) nanocomposites with the same loadings of  $\text{Ti}_3\text{C}_2\text{T}_x$  and  $Fe_3O_4$ . Meantime, the corresponding BTFCA/epoxy nanocomposites also present excellent thermal stability ( $T_{\text{heat-resistance index}}$  of 198.7 °C) and mechanical properties (storage modulus of 9902.1 MPa, Young's modulus of 4.51 GPa and hardness of 0.34 GPa). Our fabricated BTFCA/epoxy nanocomposites would greatly expand the applications of MXene and epoxy resins in the fields of information security, aerospace and weapon manufacturing, etc.



**KEYWORDS** Electromagnetic interference shielding; Epoxy nanocomposites;  $\text{Ti}_3\text{C}_2\text{T}_x$ ;  $Fe_3O_4$ ; Bidirectionally aligned three-dimensional conductive networks

✉ Hua Qiu, [huaqiu@nwpu.edu.cn](mailto:huaqiu@nwpu.edu.cn); Junwei Gu, [gjw@nwpu.edu.cn](mailto:gjw@nwpu.edu.cn); [nwpugjw@163.com](mailto:nwpugjw@163.com)

<sup>1</sup> Shaanxi Key Laboratory of Catalysis, School of Chemistry & Environment Science, Shaanxi University of Technology, Hanzhong 723001, People's Republic of China

<sup>2</sup> Shaanxi Key Laboratory of Macromolecular Science and Technology, School of Chemistry and Chemical Engineering, Northwestern Polytechnical University, Xi'an 710072, People's Republic of China



## 1 Introduction

With the rapid development of modern electronic information technology, especially for aerospace weapons and equipment technology, electromagnetic interference (EMI) pollution problem caused by high-frequency and high-power electronic equipment is becoming increasingly serious. It poses serious threats to normal operation of precise electronic components and human health [1–3]. Polymer matrix EMI shielding composites have gradually become the most promising EMI shielding materials due to their advantages of lightweight, excellent specific strength, low cost, easy processing and adjustable performances [4–6].

To our knowledge, polymer matrix EMI shielding composites have achieved satisfactory EMI shielding performances by adding highly conductive and/or magnetic fillers [7–9]. The commonly used conductive fillers are metal, conductive polymers and inorganic nonmetallic materials [10, 11]. Among them, inorganic nonmetallic materials such as the graphite [12], carbon nanotubes (CNT) [13, 14], graphene [15–17] and MXene [18–20] are currently the focus of most attention, due to their advantages of high specific strength, low density, superior electrical conductivity ( $\sigma$ ) and easy processing, etc. Herein,  $\text{Ti}_3\text{C}_2\text{T}_x$  has been widely applied in the field of EMI shielding due to mature preparation technology and superior  $\sigma$  value [21–23]. However,  $\text{Ti}_3\text{C}_2\text{T}_x$  nanosheets tend to agglomerate in polymer matrix, and have large contact resistance between the nanosheets, leading to higher percolating threshold of the composites [24–26], which would cause machining difficulty and poor mechanical properties [27, 28].

Researches show that construction of three-dimensional (3D) conductive networks is proved to be an effective way to synchronously realize the excellent  $\sigma$ , EMI shielding effectiveness (EMI SE) and mechanical properties of polymer composites at relatively low  $\text{Ti}_3\text{C}_2\text{T}_x$  loadings [29–31]. Shi et al. [32] prepared  $\text{Ti}_3\text{C}_2\text{T}_x$  aerogel by freeze-drying method, and further impregnated epoxy resins to prepare  $\text{Ti}_3\text{C}_2\text{T}_x$  aerogel/epoxy composites. When the volume fraction of  $\text{Ti}_3\text{C}_2\text{T}_x$  was 0.40 vol%, the EMI SE of  $\text{Ti}_3\text{C}_2\text{T}_x$  aerogel/epoxy composites was 35 dB. Sun et al. [33] prepared  $\text{PS@Ti}_3\text{C}_2\text{T}_x$  composites by electrostatic self-assembly and molding method. When the mass fraction of  $\text{Ti}_3\text{C}_2\text{T}_x$  was

4.0 wt%,  $\sigma$  and EMI SE of  $\text{PS@Ti}_3\text{C}_2\text{T}_x$  composites were  $1081 \text{ S m}^{-1}$  and 54 dB, respectively. In our previous work, Gu et al. [34] obtained cellulose-derived carbon aerogel@reduced graphene oxide aerogels (CCA@rGO) by freeze-drying and thermal reduction, and further prepared CCA@rGO/polydimethylsiloxane (PDMS) composites by vacuum-assisted impregnation of PDMS. When the mass fraction of CCA@rGO was 3.05 wt%, the  $\sigma$  and EMI SE of the obtained CCA@rGO/PDMS composites reached  $75 \text{ S m}^{-1}$  and 51 dB, respectively.

Compared with the randomly dispersed 3D conductive networks, the aligned 3D conductive networks are not only conducive to further improving the  $\sigma$  [35–37], but also can make efficient utilization of the conductive fillers/polymer interfaces to enhance the reflection and reabsorption of electromagnetic waves [38–40]. Wu et al. [41] prepared  $\text{Ti}_3\text{C}_2\text{T}_x$  foams by directional freezing and further impregnated PDMS to prepare  $\text{Ti}_3\text{C}_2\text{T}_x$  foam/PDMS composites. When the mass fraction of  $\text{Ti}_3\text{C}_2\text{T}_x$  was 6.1 wt%, the  $\sigma$  and EMI SE of  $\text{Ti}_3\text{C}_2\text{T}_x$  foam/PDMS composites were  $2211 \text{ S m}^{-1}$  and 54 dB, respectively. Zhao et al. [15] prepared  $\text{Ti}_3\text{C}_2\text{T}_x$ /graphene hybrid aerogels (MGA) by directional freezing, and further impregnated epoxy resins to prepare MGA/epoxy composites. When the volume fraction of graphene and  $\text{Ti}_3\text{C}_2\text{T}_x$  was 0.18 and 0.74 vol%, the  $\sigma$  and EMI SE of MGA/epoxy composites were up to  $695.9 \text{ S m}^{-1}$  and 50 dB, respectively. Compared with the directional aligned 3D conductive networks, the bidirectional aligned 3D conductive networks can further reduce the percolating threshold and enhance the attenuation of electromagnetic waves by taking advantage of more regular internal interfaces [42–44]. Han et al. [45] prepared  $\text{Ti}_3\text{C}_2\text{T}_x$  foams by bidirectional freezing method. The density of  $\text{Ti}_3\text{C}_2\text{T}_x$  foams was only  $11.0 \text{ mg cm}^{-3}$ , EMI SE and SE/density (SSE) reached 71 dB and  $8818 \text{ dB cm}^3 \text{ g}^{-1}$  respectively, which exceeded the shielding performances of most reported foams. Sambyal et al. [46] prepared  $\text{Ti}_3\text{C}_2\text{T}_x$ /CNT foams by bidirectional freezing method. Results showed that the EMI SE of  $\text{Ti}_3\text{C}_2\text{T}_x$ /CNT foams (with density of only  $2.5 \text{ mg cm}^{-3}$ ) was up to 78 dB. Bidirectional aligned 3D  $\text{Ti}_3\text{C}_2\text{T}_x$  foam and  $\text{Ti}_3\text{C}_2\text{T}_x$ /CNT foam have been reported to exhibit excellent EMI shielding performances, but relatively poor mechanical properties have limited their

broader applications. Cellulose nanofibers (CNF) possess excellent mechanical properties [47, 48], and could be employed to construct bidirectional aligned 3D conductive networks with  $\text{Ti}_3\text{C}_2\text{T}_x$  via bidirectional freezing method by hydrogen bonds, which would be favor of enhancing the mechanical properties of  $\text{Ti}_3\text{C}_2\text{T}_x$  foams [49–51].

In addition, for common polymer matrix EMI shielding composites, most electromagnetic waves are reflected at the interfaces between composites and air due to impedance mismatch, which would cause electromagnetic pollution to the service environment [52–54]. Researches show that the introduction of magnetic materials would improve the impedance matching of composites and air, weaken the reflection of electromagnetic waves, and absorb electromagnetic waves through magnetic loss [55–57]. Among commonly magnetic fillers,  $\text{Fe}_3\text{O}_4$  shows great application potential in EMI shielding materials due to excellent magnetism and low cost [58–60].

In this work,  $\text{Ti}_3\text{C}_2\text{T}_x$  and  $\text{Fe}_3\text{O}_4$  were firstly assembled by electrostatic interaction, followed by combined with CNF through hydrogen bonding, and bidirectional aligned  $\text{Ti}_3\text{C}_2\text{T}_x@Fe_3O_4/CNF$  aerogels (BTFCFA) were then prepared by bidirectional freezing and freeze-drying technique. Finally, the BTFCFA/epoxy nanocomposites were prepared by vacuum-assisted impregnation of epoxy resins. Structures and morphologies of BTFCFA were characterized by X-ray diffraction (XRD), Raman spectroscopy, X-ray photoelectron spectroscopy (XPS), transmission electron microscopy (TEM) and scanning electron microscopy (SEM). Furthermore, the effects of  $\text{Fe}_3\text{O}_4$  loadings on  $\sigma$ , EMI SE, thermal stabilities and mechanical properties of the BTFCFA/epoxy nanocomposites were analyzed in detail, and the corresponding EMI shielding mechanism was investigated.

## 2 Experimental Section

### 2.1 Fabrication of BTFCFA

$\text{Fe}_3\text{O}_4$  was positively modified by CTAB, followed by mixing with  $\text{Ti}_3\text{C}_2\text{T}_x$  dispersion and freeze-dried ( $-30\text{ }^\circ\text{C}$ ,  $< 2\text{ Pa}$ ) for 36 h to get  $\text{Ti}_3\text{C}_2\text{T}_x@Fe_3O_4$  hybrid.

Different contents of  $\text{Ti}_3\text{C}_2\text{T}_x@Fe_3O_4$  were dispersed in 10 mL of  $2.5\text{ mg mL}^{-1}$  CNF in a glass vessel by a probe sonication for 10 min in an ice bath, followed by vigorous stirring for 3 h. Then the dispersion was poured in a square mold (side length of 3 cm, height of 5 cm, PDMS wedge with a slope angle of around  $15^\circ$  at the bottom, copper as bottom, nylon as wall), and liquid nitrogen ( $-196\text{ }^\circ\text{C}$ ) was used to freeze the bottom of the cylindrical mold through the intermediary of copper blocks. BTFCFA was obtained by freeze-drying at  $-60\text{ }^\circ\text{C}$  with pressure less than 5 Pa, followed by annealed at  $400\text{ }^\circ\text{C}$  for 2 h at a heating rate of  $5\text{ }^\circ\text{C s}^{-1}$  in an Ar + 5%  $\text{H}_2$  ambient.  $\text{Ti}_3\text{C}_2\text{T}_x$  content was fixed as 400 mg, the weight ratio of  $\text{Ti}_3\text{C}_2\text{T}_x/Fe_3O_4$  was 4/1, 2/1, 1/1, and 1/2, respectively, and the corresponding samples were marked as BTFCFA-1, BTFCFA-2, BTFCFA-3 and BTFCFA-4. For comparison, the bidirectional  $\text{Ti}_3\text{C}_2\text{T}_x/CNF$  aerogels (BTCA) were also prepared.

### 2.2 Fabrication of BTFCFA/epoxy Nanocomposites

Epon 862 and diethyl methyl benzene diamine were firstly stirred at  $70\text{ }^\circ\text{C}$  for 1 h, and then filled into BTFCFA via vacuum-assisted impregnation technique. Finally, BTFCFA/epoxy nanocomposites were prepared by heating at  $120\text{ }^\circ\text{C}$  for 5 h. For comparison, BTCA/epoxy nanocomposites were prepared by the same process. Figure 1 is the schematic diagram of preparation for BTFCFA/epoxy nanocomposites.

## 3 Results and Discussion

### 3.1 Characterization of BTCA and BTFCFA

In Fig. S1,  $\text{Ti}_3\text{AlC}_2$  precursor with dense layered structure (Fig. S1a) is exfoliated into few-layered  $\text{Ti}_3\text{C}_2\text{T}_x$  nanosheets (Fig. S1b). In Fig. S2,  $\text{Fe}_3\text{O}_4$  presents (220), (311), (400), (422), (511), and (440) diffraction peaks [61], and corresponding saturation magnetization is  $70\text{ emu g}^{-1}$ . After electrostatic assembly,  $\text{Fe}_3\text{O}_4$  is uniformly dispersed on  $\text{Ti}_3\text{C}_2\text{T}_x$  nanosheets to obtain  $\text{Ti}_3\text{C}_2\text{T}_x@Fe_3O_4$  (Fig. S3). Figure 2 shows XRD, Raman, XPS spectra and hysteresis loops of BTCA and BTFCFA-2. From Fig. 2a,

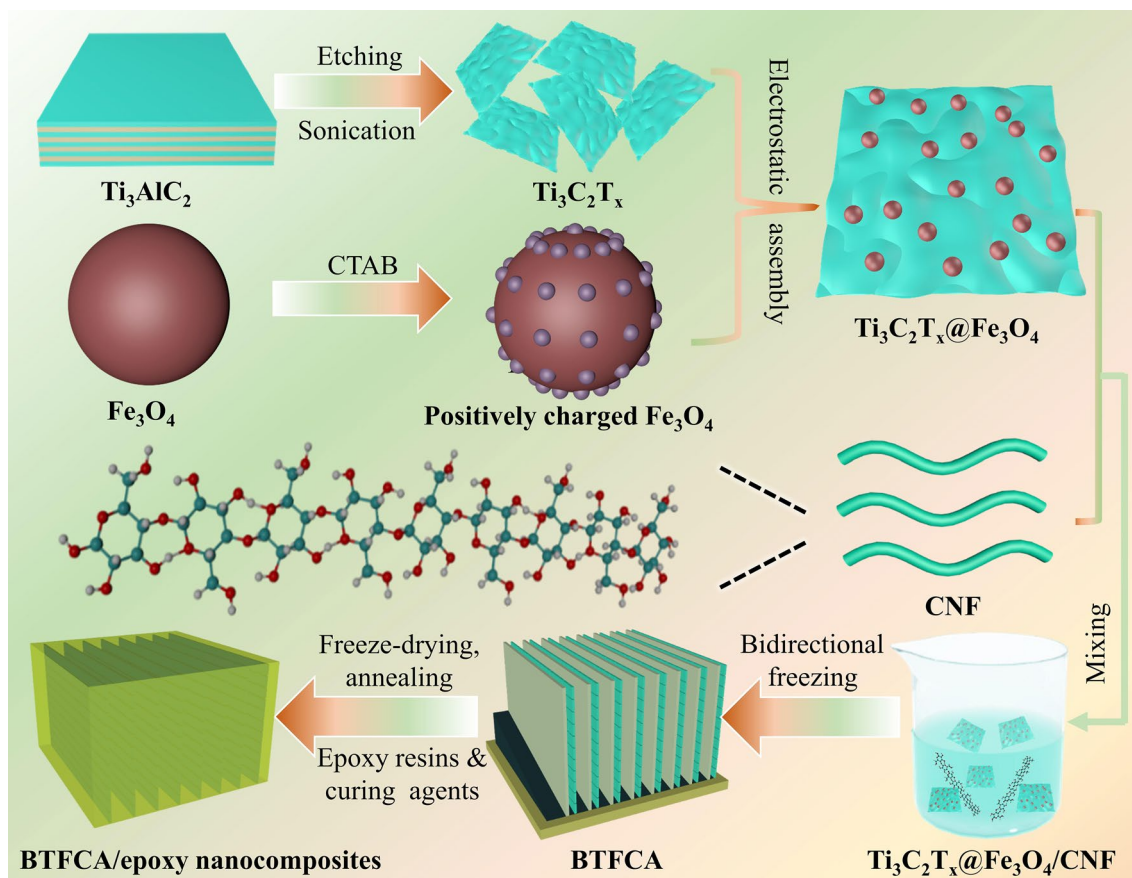


**Fig. 1** Schematic illustration of fabrication process for BTFCAs/epoxy nanocomposites

BTCA shows diffraction peaks at  $6.2^\circ$  and  $23^\circ$  corresponding to (002) lattice plane of  $\text{Ti}_3\text{C}_2\text{T}_x$  and (002) lattice plane of CNF [62]. After  $\text{Fe}_3\text{O}_4$  is introduced, three new diffraction peaks appear at  $36.7^\circ$ ,  $43.6^\circ$ , and  $63.8^\circ$  of BTFCAs-2, corresponding to the (311), (400) and (440) crystal planes of  $\text{Fe}_3\text{O}_4$ , respectively. As observed in Fig. 2b, BTCA has D-band and G-band at  $1355$  and  $1583\text{ cm}^{-1}$ , which are attributed to the graphitized structures [63, 64] formed after thermal reduction of CNF, and characteristic peaks of  $\text{Ti}_3\text{C}_2\text{T}_x$  appear within  $100\sim 700\text{ cm}^{-1}$ . Peak at  $198\text{ cm}^{-1}$  is attributed to  $A_{1g}$  symmetry out-of-plane vibration of Ti atom. Peaks at  $374$  and  $583\text{ cm}^{-1}$  are ascribed to the  $E_g$  group vibration and in-plane (shear) modes of Ti, C, and surface functional groups [65]. After  $\text{Fe}_3\text{O}_4$  is introduced, a new peak appears in BTFCAs-2 at  $655\text{ cm}^{-1}$ , which is attributed to the vibration of  $\text{Fe}_3\text{O}_4$  in  $A_{1g}$  mode. As shown in Fig. 2c, BTCA presents peaks of Ti  $3p$ , Ti  $3s$ ,

C  $1s$ , Ti  $2p$ , O  $1s$ , Ti  $2s$ , and F  $1s$  at 35, 60, 287, 457, 531, 563, and 685 eV [66]. After  $\text{Fe}_3\text{O}_4$  is introduced, BTFCAs-2 shows two new peaks at 709 and 723 eV, which are attributed to Fe  $2p_{3/2}$  and Fe  $2p_{1/2}$ , respectively. From Fig. 2d, the saturation magnetization of BTCA is 0, and the saturation magnetization of BTFCAs-2 significantly improves to  $16.7\text{ emu g}^{-1}$ . XRD, Raman spectroscopy, XPS and hysteresis loops indicate that BTFCAs has been successfully prepared.

### 3.2 Morphologies of BTFCAs and BTFCAs/epoxy Nanocomposites

Figure 3 is the SEM images of BTCA and BTFCAs, as well as the photo of BTFCAs-2 attracted on the magnet. From Fig. 3a,  $\text{Ti}_3\text{C}_2\text{T}_x$  and CNF in BTCA support each

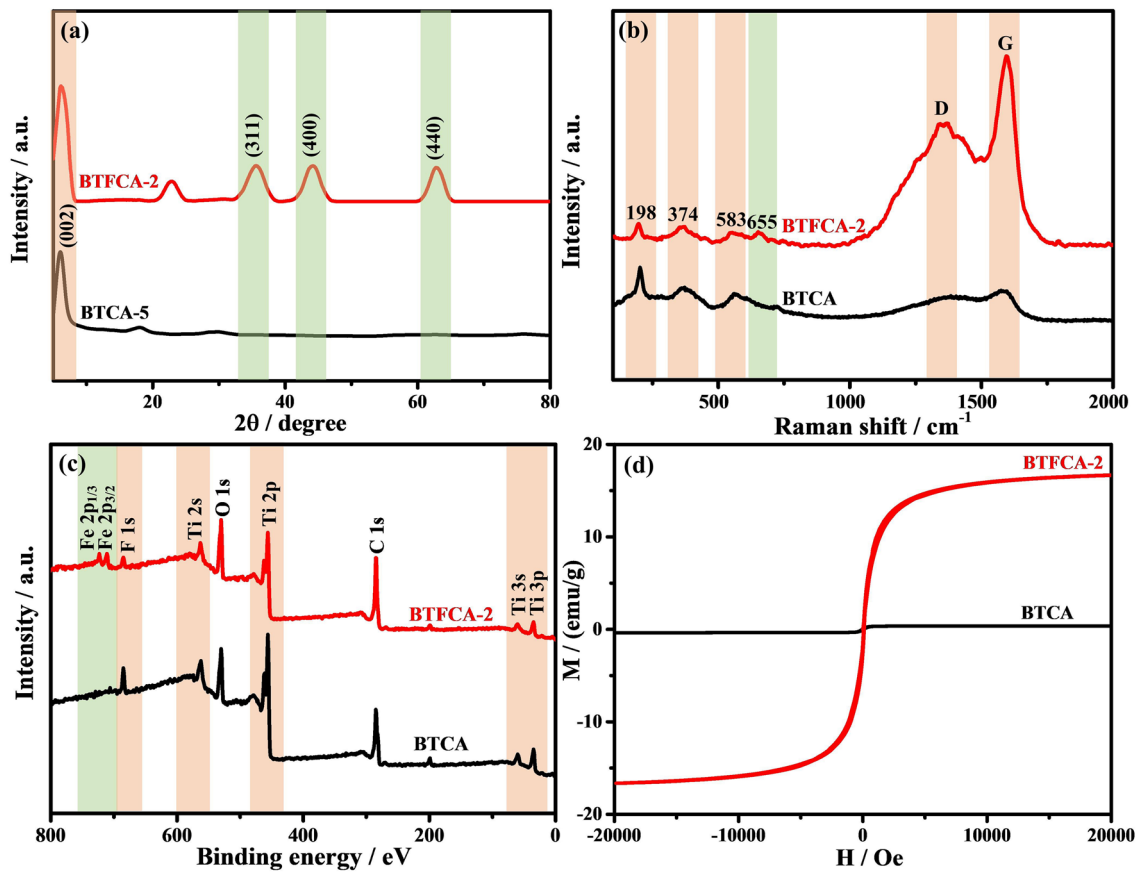


**Fig. 2** a XRD, b Raman, c XPS spectra and d hysteresis loops of BTCA and BTFCAs-2

other, to form the long-range aligned lamellar structures. After Fe<sub>3</sub>O<sub>4</sub> is introduced, BTFCAs still maintains the long-range aligned lamellar structures. With low loadings of Fe<sub>3</sub>O<sub>4</sub>, the cell size of BTFCAs increases slightly (Fig. 3b-c). However, with the excessive loadings of Fe<sub>3</sub>O<sub>4</sub>, the cell size of BTFCAs increases significantly (Fig. 3d-e). The reason is that, in bidirectional freezing process, the temperature difference makes ice crystals grow orderly in both radial and axial directions at the same time. Ti<sub>3</sub>C<sub>2</sub>T<sub>x</sub>, Fe<sub>3</sub>O<sub>4</sub> and CNF are forced to align along the direction of ice crystal growth. After removal of ice crystals by freeze-drying, the long-range aligned lamellar structures are formed in BTFCAs. The addition of Fe<sub>3</sub>O<sub>4</sub> would destroy the hydrogen bonds between Ti<sub>3</sub>C<sub>2</sub>T<sub>x</sub> and CNF to some extent. With low loadings of Fe<sub>3</sub>O<sub>4</sub>, Ti<sub>3</sub>C<sub>2</sub>T<sub>x</sub> and CNF still form abundant hydrogen bonding to maintain the long-range aligned lamellar structures, only causing slight increase in cell size of BTFCAs. The addition of excessive Fe<sub>3</sub>O<sub>4</sub> would damage the hydrogen

bonds between Ti<sub>3</sub>C<sub>2</sub>T<sub>x</sub> and CNF, which reduces the overlap between Ti<sub>3</sub>C<sub>2</sub>T<sub>x</sub> and CNF, resulting in great increase in cell size of BTFCAs. In addition, BTFCAs-2 can overcome its own gravity by magnetic force and attract to the magnet (Fig. 3f), indicating that the introduction of Fe<sub>3</sub>O<sub>4</sub> endows BTFCAs with outstanding magnetism. Figure S4 shows the SEM images of BTCA/epoxy and BTFCAs-2/epoxy nanocomposites. Both BTCA/epoxy and BTFCAs-2/epoxy nanocomposites can well maintain the original long-range aligned lamellar structures, indicating that the mechanical properties are strong enough to resist the adhesion force generated by impregnation of epoxy resins and maintain the structural integrity. On the one hand, Ti<sub>3</sub>C<sub>2</sub>T<sub>x</sub> nanosheets and CNF possess numbers of polar functional groups such as -OH and -F on the surface to form abundant hydrogen bonds, which is conducive to enhancing the stiffness of BTFCAs. On the other hand, the high rigidity of Ti<sub>3</sub>C<sub>2</sub>T<sub>x</sub> nanosheets and Fe<sub>3</sub>O<sub>4</sub> also endows BTFCAs with great rigidity, which enables

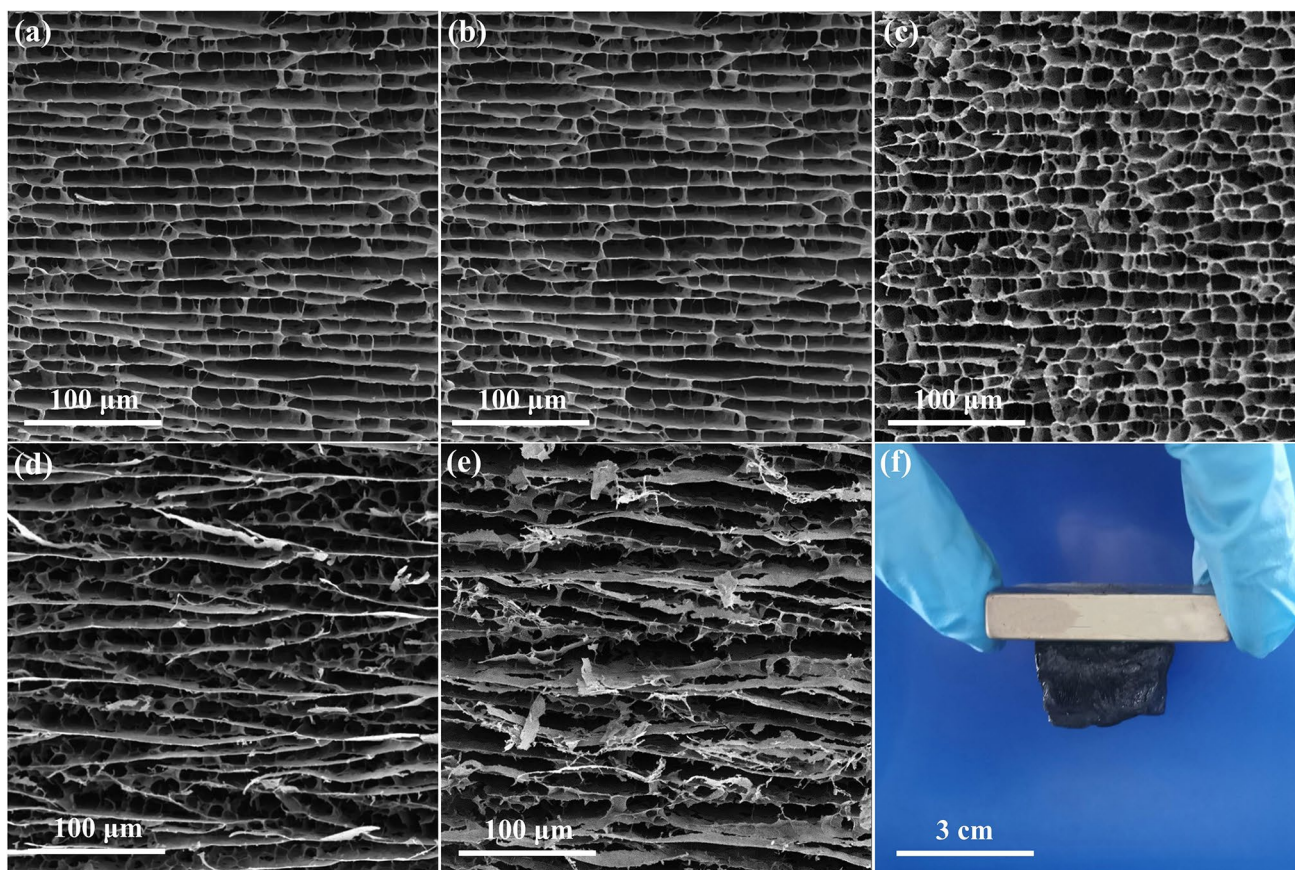


**Fig. 3** a SEM images of BTCA, b BTFCA-1, c BTFCA-2, d BTFCA-3 and e BTFCA-4. f Digital photograph of magnet attracting BTFCA-2

BTFCA/epoxy nanocomposites to maintain the integrity of the long-range aligned lamellar structures.

### 3.3 $\sigma$ and EMI Shielding Performances of BTFCA/epoxy Nanocomposites

Figure 4a shows the  $\sigma$  of BTCA/epoxy and BTFCA/epoxy nanocomposites, and the relevant values are shown in Tab S1. The  $\sigma$  of BTFCA/epoxy nanocomposites decreases gradually with increasing loadings of  $\text{Fe}_3\text{O}_4$ . When the mass fraction of  $\text{Fe}_3\text{O}_4$  is 1.48 wt%, the  $\sigma$  of BTFCA-2/epoxy nanocomposites is  $1235 \text{ S m}^{-1}$ , lower than that of BTCA/epoxy ( $1306 \text{ S m}^{-1}$ ) nanocomposites, and also significantly higher than that of blended  $\text{Ti}_3\text{C}_2\text{T}_x@ \text{Fe}_3\text{O}_4/\text{epoxy}$  ( $7.6 \text{ S m}^{-1}$ , Tab. S1) nanocomposites with the same loadings of  $\text{Ti}_3\text{C}_2\text{T}_x$  and  $\text{Fe}_3\text{O}_4$ . Highly conductive  $\text{Ti}_3\text{C}_2\text{T}_x$  nanosheets are aligned along the axial and radial directions in BTCA and BTFCA to construct a bidirectional aligned

3D conductive network, which enhances the contact among  $\text{Ti}_3\text{C}_2\text{T}_x$  nanosheets and forms abundant conductive paths, thus showing outstanding  $\sigma$ . The introduction of  $\text{Fe}_3\text{O}_4$  would affect the contact among  $\text{Ti}_3\text{C}_2\text{T}_x$  nanosheets and hinder formation of  $\text{Ti}_3\text{C}_2\text{T}_x$ - $\text{Ti}_3\text{C}_2\text{T}_x$  conductive paths, leading to slightly reduced  $\sigma$  of BTFCA/epoxy nanocomposites. The addition of excessive  $\text{Fe}_3\text{O}_4$  reduces the overlap among  $\text{Ti}_3\text{C}_2\text{T}_x$  nanosheets and significantly increases the cell size of BTFCA, which severely restricts the formation of bidirectional aligned 3D conductive networks for BTFCA, resulting in significant decrease of  $\sigma$ .

Figure 4b illustrates EMI SE of BTCA/epoxy and BTFCA/epoxy nanocomposites. The EMI SE of BTFCA/epoxy nanocomposites increases first and then decreases with increasing loadings of  $\text{Fe}_3\text{O}_4$ . When the mass fraction of  $\text{Fe}_3\text{O}_4$  is 1.48 wt%, EMI SE of BTFCA-2/epoxy nanocomposites is 79 dB, 11.3% higher than that of BTCA/epoxy (71 dB) nanocomposites, and also about 10 times that of blended  $\text{Ti}_3\text{C}_2\text{T}_x@ \text{Fe}_3\text{O}_4/\text{epoxy}$  (8 dB, Fig. S5) nanocomposites with the same

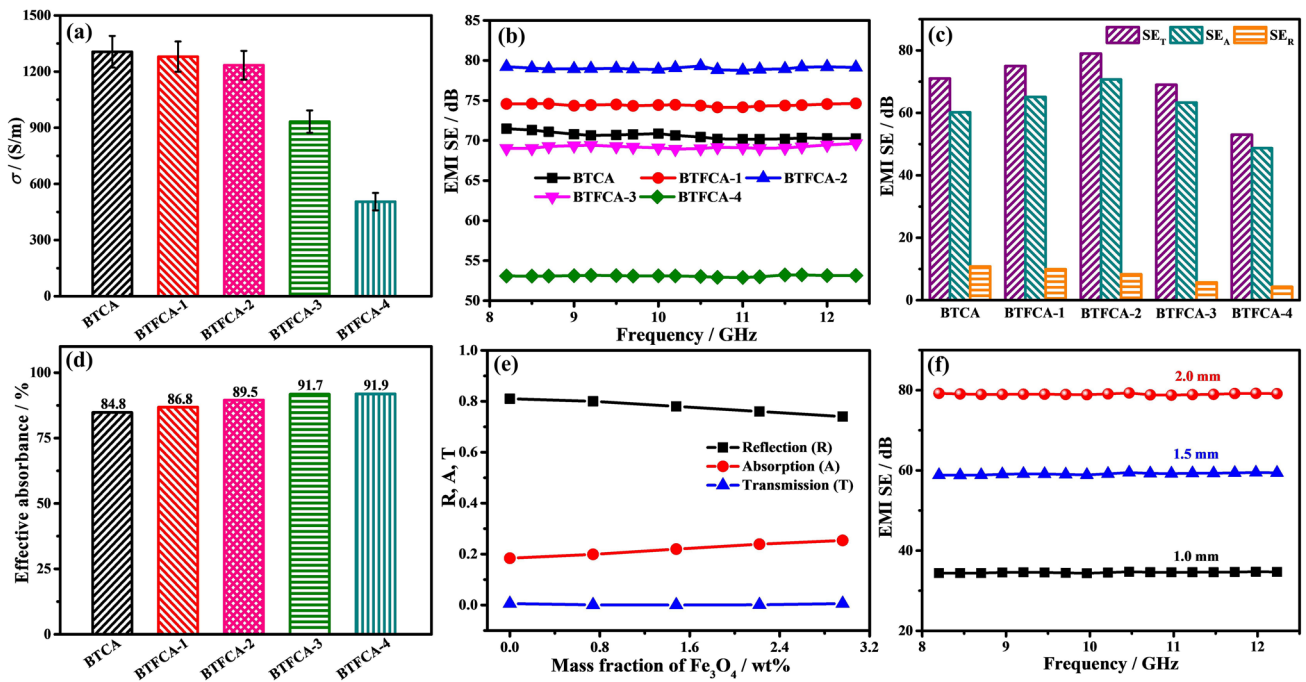


**Fig. 4** a  $\sigma$ , b EMI SE, c corresponding  $SE_T$ ,  $SE_A$ ,  $SE_R$ , d effective absorbance and e R, A, T coefficients of BTCA/epoxy and BTFCA/epoxy nanocomposites. f EMI SE of BTFCA-2/epoxy nanocomposites in different thicknesses

loadings of  $Ti_3C_2T_x$  and  $Fe_3O_4$ . The bidirectional aligned 3D conductive networks of BTFCA/epoxy nanocomposites provide abundant moving loads such as charge carriers. Under alternating electric field, they can induce microcurrent to form electrical loss through tunneling effect and other ways, and convert the energy of electromagnetic waves into heat. At the same time, the internal complex heterogeneous interfaces in BTFCA/epoxy nanocomposites extend the transmission paths of electromagnetic waves, which are conducive to enhancing the scattering and reabsorption of electromagnetic waves and further dissipating electromagnetic waves. After introduction of  $Fe_3O_4$ , reduced overlaps among  $Ti_3C_2T_x$  nanosheets lead to gradually decreased  $\sigma$  of BTFCA/epoxy nanocomposites and weakened electrical loss (such as ohmic loss) is not conducive to improvement of EMI SE. On the other hand, BTFCA/epoxy nanocomposites construct 3D magnetic networks, which enhances the multiple reflection and reabsorption of electromagnetic waves and strengthens the magnetic hysteresis loss and other magnetic losses of electromagnetic waves, so as to improve the dissipation ability of electromagnetic waves. In addition, the introduction of  $Fe_3O_4$  brings more heterogeneous interfaces. Due to interface polarization, there are a large

number of dipoles at heterogeneous interfaces, which will cause polarization loss to electromagnetic waves and further enhance the attenuation of electromagnetic waves. As a result, BTFCA-2/epoxy nanocomposites present the best EMI shielding performances. And the corresponding schematic illustration of EMI shielding mechanism of BTFCA/epoxy nanocomposites is shown in Fig. 5.

Figure 4c is  $SE_T$ ,  $SE_A$  and  $SE_R$  of BTCA/epoxy and BTFCA/epoxy nanocomposites. With increasing loadings of  $Fe_3O_4$ ,  $SE_R$  of BTFCA/epoxy nanocomposites decreases gradually, and  $SE_A$  increases first and then decreases. When the mass fraction of  $Fe_3O_4$  is 1.48 wt%,  $SE_R$  and  $SE_A$  of BTFCA-2/epoxy nanocomposites are 8 and 71 dB respectively. With increasing loadings of  $Fe_3O_4$ , the gradually decreased  $\sigma$  of BTFCA/epoxy nanocomposites improves the impedance matching, resulting in gradual decrease of  $SE_R$ . Although the electrical loss of BTFCA/epoxy nanocomposites to electromagnetic waves is gradually weakened, the internal multiple reflection, magnetic loss and polarization loss are gradually enhanced. As a result,  $SE_A$  of BTFCA-2/epoxy nanocomposites is the maximum.

Figure 4d shows the electromagnetic wave effective absorbance of BTCA/epoxy and BTFCA/epoxy

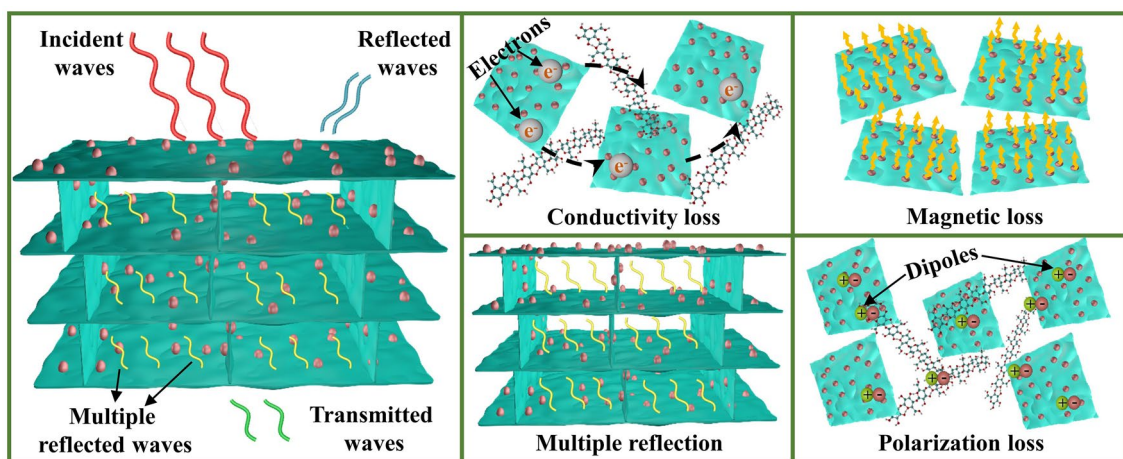


**Fig. 5** Schematic illustration of EMI shielding mechanism for BTFCa/epoxy nanocomposites

nanocomposites. With increasing loadings of  $\text{Fe}_3\text{O}_4$ , the electromagnetic wave effective absorbance of BTFCa/epoxy nanocomposites gradually increases. When the mass fraction of  $\text{Fe}_3\text{O}_4$  is 1.48 wt%, the electromagnetic wave effective absorbance of BTFCa-2/epoxy nanocomposites is 89.5%. The introduction of  $\text{Fe}_3\text{O}_4$  not only improves the impedance matching of BTFCa/epoxy nanocomposites and air, but also enhances the magnetic loss to improve the electromagnetic wave effective absorbance.

Figure 4e is the reflection ( $R$ ), absorption ( $A$ ) and transmission ( $T$ ) coefficients of BTCA/epoxy and BTFCa/epoxy nanocomposites. With increasing loadings of  $\text{Fe}_3\text{O}_4$ , the  $R$  coefficient of BTFCa/epoxy nanocomposites decreases gradually, and the  $T$  coefficient decreases first and then increases. When the mass fraction of  $\text{Fe}_3\text{O}_4$  is 1.48 wt%, the  $T$  coefficient of BTFCa-2/epoxy nanocomposites is the lowest, only  $4 \times 10^{-4}$ , and the  $R$  coefficient is 0.78. It demonstrates that the incorporation of  $\text{Fe}_3\text{O}_4$  can significantly improve the EMI shielding performances. With increasing loadings of  $\text{Fe}_3\text{O}_4$ , the  $\sigma$  of BTFCa/epoxy nanocomposites decreases gradually, which improves the impedance matching between BTFCa/epoxy nanocomposites and the air, and reduces the  $R$  coefficient gradually, thus weakening the secondary electromagnetic pollution. With introduction of  $\text{Fe}_3\text{O}_4$ , although the decreased  $\sigma$  leads to reduced electrical loss to electromagnetic waves, the internal multiple reflection, magnetic loss and interfacial polarization loss are enhanced. Under the comprehensive action, BTFCa-2/epoxy nanocomposites show the optimal EMI shielding performances and the corresponding  $T$  coefficient is the lowest.

Figure 4f demonstrates EMI SE of BTFCa-2/epoxy nanocomposites in different thicknesses, and the EMI SE of BTFCa/epoxy nanocomposites increases with increasing thicknesses. When the thickness increases from 1 to 2 mm, the EMI SE of BTFCa-2/epoxy nanocomposites increases from 34 to 79 dB. This is because the increased thickness is in favor of lengthening the propagation path of electromagnetic waves in BTFCa/epoxy nanocomposites, which is conducive to the scattering and reabsorption of electromagnetic waves to further enhance EMI shielding performances.

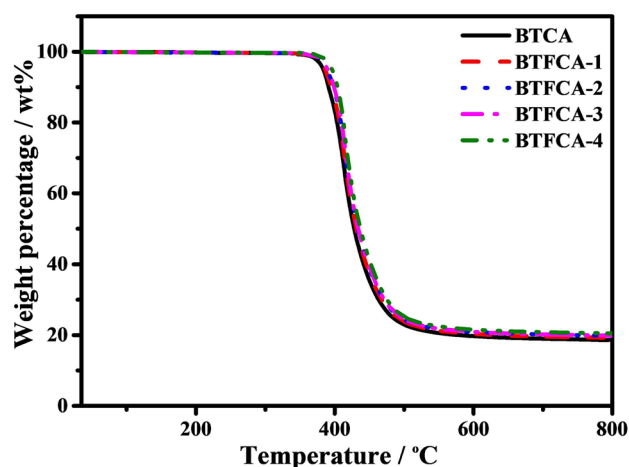


**Fig. 6** TGA curves of BTCA/epoxy and BTFCa/epoxy nanocomposites



### 3.4 Thermal Stabilities of BTFCFA/epoxy Nanocomposites

Figure 6 presents the thermogravimetric analysis (TGA) curves of BTCA/epoxy and BTFCFA/epoxy nanocomposites, and the corresponding thermal data are shown in Tab. S2.  $T_{\text{heat-resistance index}} (T_{\text{HRI}})$  can reflect the heat resistance of the materials [67]. It can be seen that  $T_{\text{HRI}}$  of BTFCFA/epoxy nanocomposites increases gradually with increasing loadings of  $\text{Fe}_3\text{O}_4$ . When the mass fraction of  $\text{Fe}_3\text{O}_4$  is 1.48 wt%,  $T_{\text{HRI}}$  of BTFCFA-2/epoxy nanocomposites is 198.7 °C, increased by 2.6 °C compared with that of BTCA/epoxy (196.1 °C) nanocomposites. The main reason is that  $\text{Fe}_3\text{O}_4$  has more excellent heat resistance and relatively lower weight loss, resulting in slightly improved thermal stabilities of BTFCFA/epoxy nanocomposites.

### 3.5 Mechanical Properties of BTFCFA/epoxy Nanocomposites

Figures 7 and S6 show storage modulus and  $\text{Tan } \delta$  of BTCA/epoxy and BTFCFA/epoxy nanocomposites, the corresponding data are given in Tab. S2. The storage modulus of BTFCFA/epoxy nanocomposites increases first and then decrease with increasing loadings of  $\text{Fe}_3\text{O}_4$ . When the mass fraction of  $\text{Fe}_3\text{O}_4$  is 1.48 wt%, the storage modulus of BTFCFA-2/epoxy nanocomposites is 9902.1 MPa, higher than that of BTCA/epoxy (9137.3 MPa) nanocomposites. It is due to that the introduction of  $\text{Fe}_3\text{O}_4$  increases the surface

roughness of BTFCFA, which is conducive to enhancing interfacial strength between BTFCFA and epoxy resins, thus improving the storage modulus. However, the addition of excessive  $\text{Fe}_3\text{O}_4$  would destroy the bidirectional aligned 3D networks of BTFCFA, leading to decreased storage modulus.

Figure 8 presents the load–displacement curves, Young’s modulus and hardness of BTCA/epoxy and BTFCFA/epoxy nanocomposites, and the corresponding data are given in Tab. S2. Young’s modulus and hardness of BTFCFA/epoxy nanocomposites increase first and then decrease with increasing loadings of  $\text{Fe}_3\text{O}_4$ . When the mass fraction of  $\text{Fe}_3\text{O}_4$  is 1.48 wt%, the Young’s modulus and hardness of BTFCFA-2/epoxy nanocomposites are 4.51 and 0.34 GPa, improved by 6.9% and 6.3% than those of BTCA/epoxy (4.23 and 0.32 GPa) nanocomposites. The reason is that the high stiffness and hardness of  $\text{Fe}_3\text{O}_4$  can improve the Young’s modulus and hardness of BTFCFA/epoxy nanocomposites. However, the addition of excessive  $\text{Fe}_3\text{O}_4$  would damage the bidirectional aligned 3D networks of BTFCFA and weaken the ability of BTFCFA/epoxy nanocomposites to resist deformation under external force, resulting in decreased Young’s modulus and hardness.

## 4 Conclusion

Bidirectional aligned BTFCFA and the corresponding BTFCFA/epoxy nanocomposites with long-range aligned lamellar structures were successfully prepared. Benefitting from the successful construction of bidirectional aligned 3D

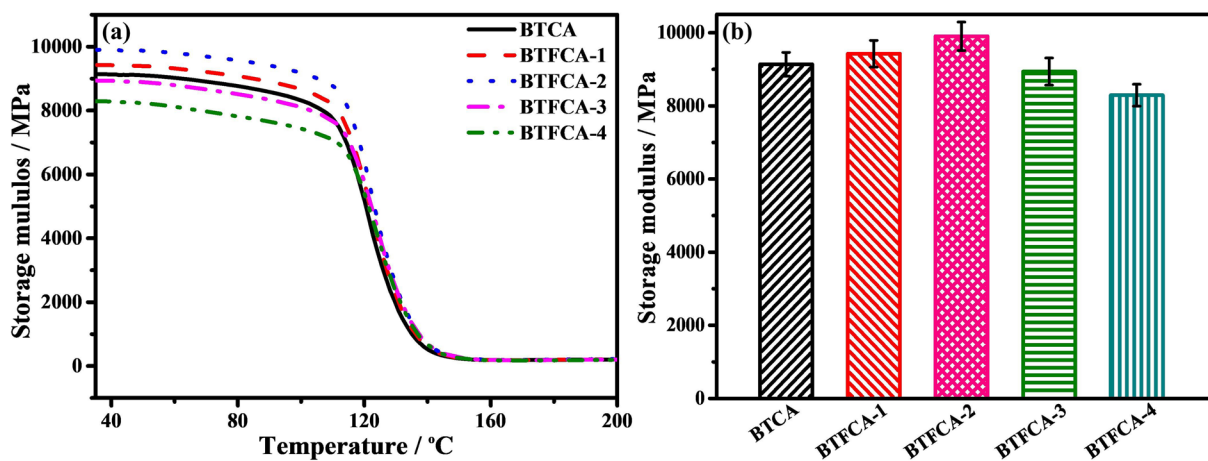
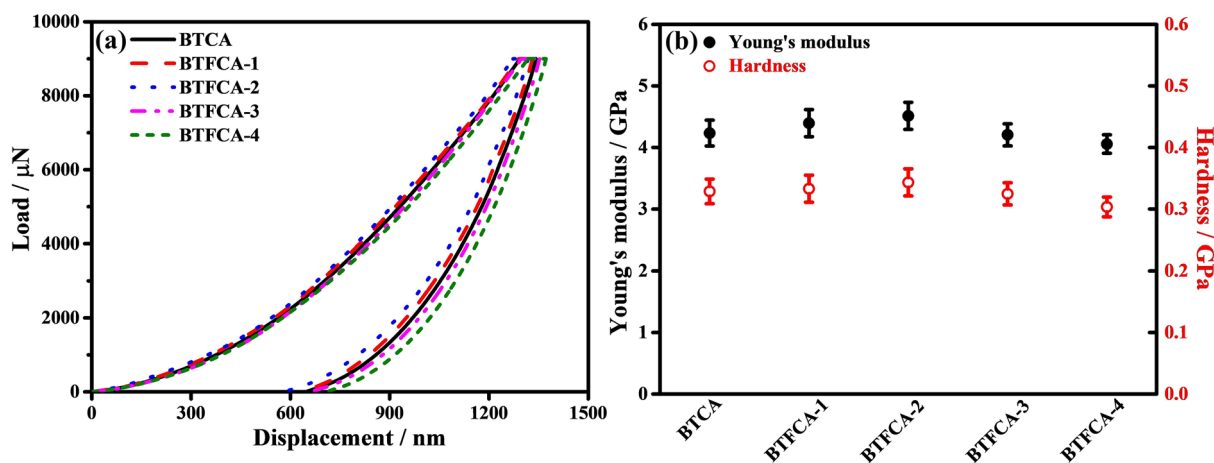


Fig. 7 a DMA curves and b storage modulus of BTCA/epoxy and BTFCFA/epoxy nanocomposites



**Fig. 8** **a** Representative load-displacements curves, **b** Young's modulus and hardness of BTCA/epoxy and BTFCA/epoxy nanocomposites

conductive networks and electromagnetic synergistic effect, when the mass fraction of  $\text{Ti}_3\text{C}_2\text{T}_x$  and  $\text{Fe}_3\text{O}_4$  is 2.96 and 1.48 wt%, BTFCA/epoxy nanocomposites show outstanding EMI SE of 79 dB, about 10 times of that of blended  $\text{Ti}_3\text{C}_2\text{T}_x@ \text{Fe}_3\text{O}_4/\text{epoxy}$  (8 dB) nanocomposites with the same loadings of  $\text{Ti}_3\text{C}_2\text{T}_x$  and  $\text{Fe}_3\text{O}_4$ . Moreover, BTFCA/epoxy nanocomposites also present excellent thermal stability ( $T_{\text{HRI}}$  of 198.7 °C) and mechanical properties (storage modulus of 9902.1 MPa, Young's modulus of 4.51 GPa, and hardness of 0.34 GPa). The obtained BTFCA/epoxy nanocomposites would greatly expand the applications of MXene and epoxy resins in the fields of information security, aerospace and weapon manufacturing, etc.

**Acknowledgements** The authors are grateful for the supports from the National Natural Science Foundation of China (U21A2093 and 52203100). Y.L. Zhang would like to thank the Innovation Foundation for Doctor Dissertation of Northwestern Polytechnical University (CX2021107). This work is also financially supported by Polymer Electromagnetic Functional Materials Innovation Team of Shaanxi Sanqin Scholars. We would also like to thank the Analytical & Testing Center of Northwestern Polytechnical University for SEM and TEM tests.

**Funding** Open access funding provided by Shanghai Jiao Tong University.

**Open Access** This article is licensed under a Creative Commons Attribution 4.0 International License, which permits use, sharing, adaptation, distribution and reproduction in any medium or format, as long as you give appropriate credit to the original author(s) and the source, provide a link to the Creative Commons licence, and indicate if changes were made. The images or other third party material in this article are included in the article's Creative

Commons licence, unless indicated otherwise in a credit line to the material. If material is not included in the article's Creative Commons licence and your intended use is not permitted by statutory regulation or exceeds the permitted use, you will need to obtain permission directly from the copyright holder. To view a copy of this licence, visit <http://creativecommons.org/licenses/by/4.0/>.

**Supplementary Information** The online version contains supplementary material available at <https://doi.org/10.1007/s40820-022-00949-8>.

## References

1. F. Shahzad, M. Alhabeb, C. Hatter, B. Anasori, S.M. Hong et al., Electromagnetic interference shielding with 2D transition metal carbides (MXenes). *Science* **353**(6304), 1137–1140 (2016). <https://doi.org/10.1126/science.aag2421>
2. T. Wang, W.W. Kong, W.C. Yu, J.F. Gao, K. Dai et al., A healable and mechanically enhanced composite with segregated conductive network structure for high-efficient electromagnetic interference shielding. *Nano. Micro. Lett.* **13**, 162 (2021). <https://doi.org/10.1007/s40820-021-00693-5>
3. Y. Zhang, J. Kong, J. Gu, New generation electromagnetic materials: harvesting instead of dissipation solo. *Sci. Bull.* **67**, 1413–1415 (2022). <https://doi.org/10.1016/j.scib.2022.06.017>
4. Y.J. Mao, L. Xu, H. Lin, J. Li, D.X. Yan et al., Effective electromagnetic interference shielding properties of micro-truss structured CNT/epoxy composites fabricated based on visible light processing. *Compos. Sci. Technol.* **221**, 109296 (2022). <https://doi.org/10.1016/j.compscitech.2022.109296>
5. D.X. Yan, H. Pang, B. Li, R. Vajtai, L. Xu et al., Structured reduced graphene oxide/polymer composites for ultra-efficient electromagnetic interference shielding. *Adv. Funct. Mater.*

- 25(4), 559–566 (2015). <https://doi.org/10.1002/adfm.201403809>
6. Y. Zhang, J. Gu, A perspective for developing polymer-based electromagnetic interference shielding composites. *Nano. Micro Lett.* **14**, 89 (2022). <https://doi.org/10.1007/s40820-022-00843-3>
  7. F. Xie, F. Jia, L. Zhuo, Z. Lu, L. Si et al., Ultrathin MXene/aramid nanofiber composite paper with excellent mechanical properties for efficient electromagnetic interference shielding. *Nanoscale* **11**(48), 23382–23391 (2019). <https://doi.org/10.1039/c9nr07331k>
  8. R. Liu, M. Miao, Y. Li, J. Zhang, S. Cao et al., Ultrathin biomimetic polymeric  $Ti_3C_2T_x$  MXene composite films for electromagnetic interference shielding. *ACS Appl. Mater. Interfaces* **10**(51), 44787–44795 (2018). <https://doi.org/10.1021/acsami.8b18347>
  9. P. Hu, J. Lyu, C. Fu, W. Gong, J. Liao et al., Multifunctional aramid nanofiber/carbon nanotube hybrid aerogel films. *ACS Nano* **14**(1), 688–697 (2019). <https://doi.org/10.1021/acsnano.9b07459>
  10. C.B. Li, Y.J. Li, Q. Zhao, Y. Luo, G.Y. Yang et al., Electromagnetic interference shielding of graphene aerogel with layered microstructure fabricated via mechanical compression. *ACS Appl. Mater. Interfaces* **12**(27), 30686–30694 (2020). <https://doi.org/10.1021/acsami.0c05688>
  11. Z. Ma, X. Xiang, L. Shao, Y. Zhang, J. Gu, Multifunctional wearable silver nanowire decorated leather nanocomposites for joule heating, electromagnetic interference shielding and piezoresistive sensing. *Angew. Chem. Int. Ed.* **61**(15), e202200705 (2022). <https://doi.org/10.1002/anie.202200705>
  12. Y. Li, X. Lan, F. Wu, J. Liu, P. Huang et al., Steam-chest molding of polypropylene/carbon black composite foams as broadband EMI shields with high absorptivity. *Compos. Commun.* **22**, 100508 (2020). <https://doi.org/10.1016/j.coco.2020.100508>
  13. W. Cao, C. Ma, S. Tan, M. Ma, P. Wan et al., Ultrathin and flexible CNTs/MXene/cellulose nanofibrils composite paper for electromagnetic interference shielding. *Nano-Micro Lett.* **11**, 72 (2019). <https://doi.org/10.1007/s40820-019-0304-y>
  14. J. Chen, X. Liao, W. Xiao, J. Yang, Q. Jiang et al., Facile and green method to structure ultralow-threshold and lightweight polystyrene/MWCNT composites with segregated conductive networks for efficient electromagnetic interference shielding. *ACS Sustainable Chem. Eng.* **7**(11), 9904–9915 (2019). <https://doi.org/10.1021/acssuschemeng.9b00678>
  15. S. Zhao, H.B. Zhang, J. Luo, Q. Wang, B. Xu et al., Highly electrically conductive three-dimensional  $Ti_3C_2T_x$  MXene/reduced graphene oxide hybrid aerogels with excellent electromagnetic interference shielding performances. *ACS Nano* **12**(11), 11193–11202 (2018). <https://doi.org/10.1021/acsnano.8b05739>
  16. J. Liu, Z. Liu, H.B. Zhang, W. Chen, Z. Zhao et al., Ultrastrong and highly conductive MXene-based films for high-performance electromagnetic interference shielding. *Adv. Electron. Mater.* **6**(1), 1901094 (2019). <https://doi.org/10.1002/aelm.201901094>
  17. K. Pang, X. Liu, Y. Liu, Y. Chen, Z. Xu et al., Highly conductive graphene film with high-temperature stability for electromagnetic interference shielding. *Carbon* **179**, 202–208 (2021). <https://doi.org/10.1016/j.carbon.2021.04.027>
  18. M. Ying, R. Zhao, X. Hu, Z. Zhang, W. Liu et al., Wrinkled titanium carbide (MXene) with surface charge polarizations through chemical etching for superior electromagnetic interference shielding. *Angew. Chem. Int. Ed.* **134**(16), e202201323 (2022). <https://doi.org/10.1002/ange.202201323>
  19. X. Jia, B. Shen, L. Zhang, W. Zheng, Construction of compressible polymer/MXene composite foams for high-performance absorption-dominated electromagnetic shielding with ultra-low reflectivity. *Carbon* **173**, 932–940 (2021). <https://doi.org/10.1016/j.carbon.2020.11.036>
  20. M. Han, C.E. Shuck, R. Rakhmanov, D. Parchment, B. Anasori, C.M. Koo, G. Friedman, Y. Gogotsi, Beyond  $Ti_3C_2T_x$ : MXenes for electromagnetic interference shielding. *ACS Nano* **14**(4), 5008–5016 (2020). <https://doi.org/10.1021/acsnano.0c01312>
  21. G.M. Weng, J. Li, M. Alhabeb, C. Karpovich, H. Wang et al., Layer-by-layer assembly of cross-functional semi-transparent MXene-carbon nanotubes composite films for next-generation electromagnetic interference shielding. *Adv. Funct. Mater.* **28**(44), 1803360 (2018). <https://doi.org/10.1002/adfm.201803360>
  22. B. Zhou, Q. Li, P. Xu, Y. Feng, J. Ma et al., An asymmetric sandwich structural cellulose-based film with self-supported MXene and AgNW layers for flexible electromagnetic interference shielding and thermal management. *ACS Appl. Mater. Interfaces* **13**(4), 2378–2388 (2021). <https://doi.org/10.1039/D0NR07840A>
  23. B. Zhou, M. Su, D. Yang, G. Han, C. Shen, Flexible MXene/silver nanowire-based transparent conductive film with electromagnetic interference shielding and electro-photo-thermal performance. *ACS Appl. Mater. Interfaces* **12**(36), 40859–40869 (2020). <https://doi.org/10.1021/acsami.0c09020>
  24. Y. Zhang, Y. Yan, H. Qiu, Z. Ma, K. Ruan et al., A mini-review of MXene porous films: preparation, mechanism and application. *J. Mater. Sci. Technol.* **103**, 42–49 (2022). <https://doi.org/10.1016/j.jmst.2021.08.001>
  25. L. Li, Y. Cao, X. Liu, J. Wang, Y. Yang et al., Multifunctional MXene-based fireproof electromagnetic shielding films with exceptional anisotropic heat dissipation capability and joule heating performance. *ACS Appl. Mater. Interfaces* **12**(24), 27350–27360 (2020). <https://doi.org/10.1021/acsami.0c05692>
  26. Q. Wei, S. Pei, X. Qian, H. Liu, Z. Liu et al., Superhigh electromagnetic interference shielding of ultrathin aligned pristine graphene nanosheets film. *Adv. Mater.* **32**(14), 1907411 (2020). <https://doi.org/10.1002/adma.201907411>
  27. N. Li, Y. Huang, F. Du, X. He, X. Lin et al., Electromagnetic interference (EMI) shielding of single-walled carbon nanotube epoxy composites. *Nano Lett.* **6**(6), 1141–1145 (2006). <https://doi.org/10.1021/nl0602589>
  28. H. Xu, X. Yin, X. Li, M. Li, S. Liang et al., Lightweight  $Ti_2CT_x$  MXene/poly(vinyl alcohol) composite foams for electromagnetic wave shielding with absorption-dominated

- feature. *ACS Appl. Mater. Interfaces* **11**(10), 10198–10207 (2019). <https://doi.org/10.1021/acsami.8b21671>
29. F. Zou, J. Chen, X. Liao, P. Song, G. Li, Efficient electrical conductivity and electromagnetic interference shielding performance of double percolated polymer composite foams by phase coarsening in supercritical CO<sub>2</sub>. *Compos. Sci. Technol.* **213**, 108895 (2021). <https://doi.org/10.1016/j.compscitech.2021.108895>
30. Z. Lin, J. Liu, W. Peng, Y. Zhu, Y. Zhao et al., Highly stable 3D Ti<sub>3</sub>C<sub>2</sub>T<sub>x</sub> MXene-based foam architectures toward high-performance terahertz radiation shielding. *ACS Nano* **14**(2), 2109–2117 (2020). <https://doi.org/10.1021/acsnano.9b08832>
31. Z. Xiang, Y. Shi, X. Zhu, L. Cai, W. Lu, Flexible and waterproof 2D/1D/0D construction of MXene-based nanocomposites for electromagnetic wave absorption, EMI shielding, and photothermal conversion. *Nano-Micro Lett.* **13**, 150 (2021). <https://doi.org/10.1007/s40820-021-00673-9>
32. S. Shi, B. Qian, X. Wu, H. Sun, H. Wang et al., Self-assembly of MXene-surfactants at liquid-liquid interfaces: from structured liquids to 3D aerogels. *Angew. Chem. Int. Ed.* **58**(50), 18171–18176 (2019). <https://doi.org/10.1002/anie.201908402>
33. R. Sun, H.B. Zhang, J. Liu, X. Xie, R. Yang et al., Highly conductive transition metal carbide/carbonitride (MXene)@ polystyrene nanocomposites fabricated by electrostatic assembly for highly efficient electromagnetic interference shielding. *Adv. Funct. Mater.* **27**(45), 1702807 (2017). <https://doi.org/10.1002/adfm.201702807>
34. P. Song, B. Liu, C. Liang, K. Ruan, H. Qiu et al., Lightweight, flexible cellulose-derived carbon aerogel@reduced graphene oxide/PDMS composites with outstanding EMI shielding performances and excellent thermal conductivities. *Nano-Micro Lett.* **13**, 91 (2021). <https://doi.org/10.1007/s40820-021-00624-4>
35. Z. Zeng, H. Jin, M. Chen, W. Li, L. Zhou et al., Lightweight and anisotropic porous MWCNT/WPU composites for ultrahigh performance electromagnetic interference shielding. *Adv. Funct. Mater.* **26**(2), 303–310 (2016). <https://doi.org/10.1002/adfm.201503579>
36. Z. Wu, T. Shang, Y. Deng, Y. Tao, Q.H. Yang, The assembly of MXenes from 2D to 3D. *Adv. Sci.* **7**(7), 1903077 (2020). <https://doi.org/10.1002/advs.201903077>
37. G.S. Lee, T. Yun, H. Kim, I.H. Kim, J. Choi et al., Mussel inspired highly aligned Ti<sub>3</sub>C<sub>2</sub>T<sub>x</sub> MXene film with synergistic enhancement of mechanical strength and ambient stability. *ACS Nano* **14**(9), 11722–11732 (2020). <https://doi.org/10.1021/acsnano.0c04411>
38. H. Liu, Z. Huang, T. Chen, X. Su, Y. Liu et al., Construction of 3D MXene/silver nanowires aerogels reinforced polymer composites for extraordinary electromagnetic interference shielding and thermal conductivity. *Chem. Eng. J.* **427**, 131540 (2022). <https://doi.org/10.1016/j.cej.2021.131540>
39. Z. Deng, P. Tang, X. Wu, H.B. Zhang, Z.Z. Yu, Superelectric, ultralight, and conductive Ti<sub>3</sub>C<sub>2</sub>T<sub>x</sub> MXene/acidified carbon nanotube anisotropic aerogels for electromagnetic interference shielding. *ACS Appl. Mater. Interfaces* **13**(17), 20539–20547 (2021). <https://doi.org/10.1021/acsami.1c02059>
40. Y. Dai, X. Wu, Z. Liu, H.B. Zhang, Z.Z. Yu, Highly sensitive, robust and anisotropic MXene aerogels for efficient broadband microwave absorption. *Compos. Part B Eng.* **200**, 108263 (2020). <https://doi.org/10.1016/j.compositesb.2020.108263>
41. X. Wu, B. Han, H.B. Zhang, X. Xie, T. Tu et al., Compressible, durable and conductive polydimethylsiloxane-coated MXene foams for high-performance electromagnetic interference shielding. *Chem. Eng. J.* **381**, 122622 (2020). <https://doi.org/10.1016/j.cej.2019.122622>
42. Z. Lu, F. Jia, L. Zhuo, D. Ning, K. Gao et al., Micro-porous MXene/Aramid nanofibers hybrid aerogel with reversible compression and efficient EMI shielding performance. *Compos. Part B Eng.* **217**, 108853 (2021). <https://doi.org/10.1016/j.compositesb.2021.108853>
43. A. Iqbal, P. Sambyal, C.M. Koo, 2D MXenes for electromagnetic shielding: a review. *Adv. Funct. Mater.* **30**(47), 2000883 (2020). <https://doi.org/10.1016/j.compositesb.2021.108853>
44. B.W. Liu, M. Cao, Y.Y. Zhang, Y.Z. Wang, H.B. Zhao, Multifunctional protective aerogel with superelasticity over -196 to 500 °C. *Nano Res.* **15**, 7797–7805 (2022). <https://doi.org/10.1007/s12274-022-4699-2>
45. M. Han, X. Yin, K. Hantanasirisakul, X. Li, A. Iqbal et al., Anisotropic MXene aerogels with a mechanically tunable ratio of electromagnetic wave reflection to absorption. *Adv. Opt. Mater.* **7**(10), 1900267 (2019). <https://doi.org/10.1002/adom.201900267>
46. P. Sambyal, A. Iqbal, J. Hong, H. Kim, M. Kim et al., Ultralight and mechanically robust Ti<sub>3</sub>C<sub>2</sub>T<sub>x</sub> hybrid aerogel reinforced by carbon nanotubes for electromagnetic interference shielding. *ACS Appl. Mater. Interfaces* **11**(41), 38046–38054 (2019). <https://doi.org/10.1021/acsami.9b12550>
47. S. Cao, X. Feng, Y. Song, X. Xue, H. Liu et al., Integrated fast assembly of free-standing lithium titanate/carbon nanotube/cellulose nanofiber hybrid network film as flexible paper-electrode for lithium-ion batteries. *ACS Appl. Mater. Interfaces* **7**(20), 10695–10701 (2015). <https://doi.org/10.1021/acsami.5b02693>
48. W. Chen, D. Zhang, K. Yang, M. Luo, P. Yang et al., MXene (Ti<sub>3</sub>C<sub>2</sub>T<sub>x</sub>)/cellulose nanofiber/porous carbon film as free-standing electrode for ultrathin and flexible supercapacitors. *Chem. Eng. J.* **413**, 127524 (2021). <https://doi.org/10.1016/j.cej.2020.127524>
49. Z. Zeng, C. Wang, G. Siqueira, D. Han, A. Huch et al., Nanocellulose-MXene biomimetic aerogels with orientation-tunable electromagnetic interference shielding performance. *Adv. Sci.* **7**(15), 2000979 (2020). <https://doi.org/10.1002/advs.202000979>
50. B. Zhou, Z. Zhang, Y. Li, G. Han, Y. Feng et al., Flexible, robust, and multifunctional electromagnetic interference shielding film with alternating cellulose nanofiber and MXene layers. *ACS Appl. Mater. Interfaces* **12**(4), 4895–4905 (2020). <https://doi.org/10.1021/acsami.9b19768>
51. H. Peng, M. He, Y. Zhou, Z. Song, Y. Wang et al., Low-temperature carbonized biomimetic cellulose nanofiber/MXene

- composite membrane with excellent microwave absorption performance and tunable absorption bands. *Chem. Eng. J.* **433**, 133269 (2022). <https://doi.org/10.1016/j.cej.2021.133269>
52. L. Li, S. Zhao, X.J. Luo, H.B. Zhang, Z.Z. Yu, Smart MXene-based Janus films with multi-responsive actuation capability and high electromagnetic interference shielding performances. *Carbon* **175**, 594–602 (2021). <https://doi.org/10.1016/j.carbon.2020.10.090>
53. C. Lei, Y. Zhang, D. Liu, K. Wu, Q. Fu, Metal-level robust, folding endurance, and highly temperature-stable MXene-based film with engineered aramid nanofiber for extreme-condition electromagnetic interference shielding applications. *ACS Appl. Mater. Interfaces* **12**(23), 26485–26495 (2020). <https://doi.org/10.1021/acsami.0c07387>
54. J. Zhang, N. Kong, S. Uzun, A. Levitt, S. Seyedin et al., Scalable manufacturing of free-standing, strong  $Ti_3C_2T_x$  MXene films with outstanding conductivity. *Adv. Mater.* **32**(23), 2001093 (2020). <https://doi.org/10.1002/adma.202001093>
55. Y. Zhang, Z. Ma, K. Ruan, J. Gu, Multifunctional  $Ti_3C_2T_x$ -( $Fe_3O_4$ /polyimide) composite films with Janus structure for outstanding electromagnetic interference shielding and superior visual thermal management. *Nano. Res.* **15**, 5601–5609 (2022). <https://doi.org/10.1007/s12274-022-4358-7>
56. N. Liu, Y. Dou, X. Zhang, L. Yu, X. Yan, Design of porous FeNi-carbon nanosheets by a double-effect synergistic strategy for electromagnetic wave absorption. *Carbon* **190**, 125–135 (2022). <https://doi.org/10.1016/j.carbon.2022.01.007>
57. Y. Zhang, K. Ruan, J. Gu, Flexible sandwich-structured electromagnetic interference shielding nanocomposite films with excellent thermal conductivities. *Small* **17**(42), 2101951 (2021). <https://doi.org/10.1002/sml.202101951>
58. V. Shukla, Role of spin disorder in magnetic and EMI shielding properties of  $Fe_3O_4$ /C/PPy core/shell composites. *J. Mater. Sci.* **55**(7), 2826–2835 (2020). <https://doi.org/10.1007/s10853-019-04198-w>
59. H. Fang, H. Guo, Y. Hu, Y. Ren, P.C. Hsu et al., In-situ grown hollow  $Fe_3O_4$  onto graphene foam nanocomposites with high EMI shielding effectiveness and thermal conductivity. *Compos. Sci. Technol.* **188**, 107975 (2020). <https://doi.org/10.1016/j.compscitech.2019.107975>
60. S. Zhu, Q. Cheng, C. Yu, X. Pan, X. Zuo et al., Flexible  $Fe_3O_4$ /graphene foam/poly dimethylsiloxane composite for high-performance electromagnetic interference shielding. *Compos. Sci. Technol.* **189**, 108012 (2020). <https://doi.org/10.1016/j.compscitech.2020.108012>
61. T. Ozkaya, M.S. Toprak, A. Baykal, H. Kavas, Y. Köseoğlu et al., Synthesis of  $Fe_3O_4$  nanoparticles at 100 C and its magnetic characterization. *J. Alloys. Compd.* **472**(2), 18–23 (2009). <https://doi.org/10.1016/j.compscitech.2020.108012>
62. C. Liu, Y. Bai, W. Li, F. Yang, G. Zhang et al., In situ growth of three-dimensional MXene/metal-organic framework composites for high-performance supercapacitors. *Angew. Chem. Int. Ed.* **134**(11), e202116282 (2022). <https://doi.org/10.1002/ange.202116282>
63. W. Dai, L. Lv, J. Lu, H. Hou, Q. Yan et al., A paper-like inorganic thermal interface material composed of hierarchically structured graphene/silicon carbide nanorods. *ACS Nano* **13**(2), 1547–1554 (2019). <https://doi.org/10.1021/acsnano.8b07337>
64. X. Chen, F. Meng, Z. Zhou, X. Tian, L. Shan et al., One-step synthesis of graphene/polyaniline hybrids by in situ intercalation polymerization and their electromagnetic properties. *Nanoscale* **6**(14), 8140–8148 (2014). <https://doi.org/10.1039/C4NR01738B>
65. M. Hu, Z. Li, T. Hu, S. Zhu, C. Zhang et al., High-capacitance mechanism for  $Ti_3C_2T_x$  MXene by in situ electrochemical Raman spectroscopy investigation. *ACS Nano* **10**(12), 11344–11350 (2016). <https://doi.org/10.1021/acsnano.6b06597>
66. C. Zhu, E. Chalmers, L. Chen, Y. Wang, B.B. Xu et al., A nature-inspired, flexible substrate strategy for future wearable electronics. *Small* **15**(35), 1902440 (2019). <https://doi.org/10.1002/sml.201902440>
67. Z. Liu, X. Fan, L. Cheng, J. Zhang, L. Tang et al., Hybrid polymer membrane functionalized PBO fibers/cyanate esters wave-transparent laminated composites. *Adv. Fiber. Mater.* **4**(3), 520–531 (2022). <https://doi.org/10.1007/s42765-021-00125-4>

